Madden–Julian Oscillation (MJO) Modulation of Atmospheric Circulation and Chilean Winter Precipitation

BRADFORD S. BARRETT

Oceanography Department, U.S. Naval Academy, Annapolis, Maryland

JORGE F. CARRASCO

Dirección Meteorológica de Chile, Santiago, Chile

ANTHONY P. TESTINO

Oceanography Department, U.S. Naval Academy, Annapolis, Maryland

(Manuscript received 18 April 2011, in final form 15 August 2011)

ABSTRACT

The leading intraseasonal mode of tropical atmospheric variability, the Madden–Julian oscillation (MJO), has been shown to modulate precipitation and circulation on a global and regional scale. Winter precipitation in Chile has been connected to a variety of synoptic-scale forcing mechanisms. This study explored the links between the two, first examining the intraseasonal variability of Chilean precipitation from surface gauges and the Tropical Rainfall Measuring Mission (TRMM) and then examining the variability of synoptic-scale circulation.

Composites of precipitation, precipitation intensity, and lower-, middle-, and upper-tropospheric circulation were created using the Real-Time Multivariate MJO index, which divides the MJO into eight longitudinally based phases. Precipitation was found to vary across MJO phases, with positive precipitation anomalies in central and south-central Chile (30°–45°S) for MJO phases 8, 1, and 2, and negative anomalies in phases 3–7. Circulation was also found to vary across phase, in good agreement with precipitation: low geopotential height and negative omega (corresponding to upward vertical motion) anomalies were found over and upstream of Chile during the rainier phases, and the anomalies reversed during the drier phases. Surface pressure and middle- and upper-tropospheric geopotential height anomalies showed a classic equivalent barotropic wave train, indicating a teleconnection response to deep convective activity in the Maritime Continent in agreement with numerous earlier observational, modeling, and theoretical studies.

1. Introduction

Madden–Julian oscillation (MJO) modulation of global and regional precipitation has been well documented (e.g., Donald et al. 2006; Jeong et al. 2008; Wheeler et al. 2009; Jones et al. 2011; Martin and Schumacher 2011). Similarly, mean circulation and forcing mechanisms during winter precipitation events in Chile have also been well studied (e.g., Barrett et al. 2011; Garreaud 2009; Barrett et al. 2009; Falvey and Garreaud 2007). The objective of this study is to connect the two as follows: to explain the observed intraseasonal variability of precipitation in Chile by examining the MJO's impact on atmospheric circulation and relevant forcing mechanisms.

The MJO (Madden and Julian 1971, 1972) is the leading mode of intraseasonal variability of the tropical atmosphere. Its most basic feature consists of a planetary-scale, eastward-moving region of deep convective clouds and heavy precipitation bounded on both the west and east by regions of suppressed convection and minimal precipitation. Zonal circulations connect the two regions, with lower troposphere (near 850 hPa) anomalous westerly (easterly) winds to the west (east) of the deep convection; in the upper troposphere (near 200 hPa), the circulation anomalies are reversed (Nogués-Paegle et al. 1989). The convective anomalies have been observed to remain between the Indian Ocean and 180° (Matthews

Corresponding author address: Bradford S. Barrett, Oceanography Department, U.S. Naval Academy, 572C Holloway Rd., Annapolis, MD 21402.
E-mail: bbarrett@usna.edu

DOI: 10.1175/JCLI-D-11-00216.1

2000), while the circulation anomalies have been observed to circumnavigate the tropics (Krishnamurti et al. 1985). Low-latitude thermal forcing, such as that produced by convection that occurs over the Maritime Continent during certain phases of the MJO, generates wave trains whose long wavelengths propagate poleward and eastward (Hoskins and Karoly 1981). It is this teleconnection to the Southern Hemisphere that is critical to explaining the link between intraseasonal precipitation variability in Chile and the MJO. A detailed review of the MJO, including discussion of its complex multiscale structure and variability with other leading atmospheric–oceanic modes such as ENSO and the seasonal cycle, is presented in Zhang (2005).

Chile is a unique country in many ways. Meteorologically, its long latitudinal extent and diverse topography combine to yield sharp gradients in climate zones. In the north, the Atacama Desert region is one of the most hyperarid locations in the world (Garreaud et al. 2010), while in the south, the lush Lakes Region and many glaciers are evidence of abundant precipitation that sometimes exceeds 6000 mm yr^{-1} (Smith and Evans 2007). Mean winter season precipitation from both surface stations (Fig. 1) and Tropical Rainfall Measuring Mission (TRMM) shows these gradients, with minimal precipitation in the north quickly transitioning to a winter maximum near 40°S before trailing off again (Fig. 2). Even with this diversity, however, many authors who have studied Chilean precipitation have pointed to similar synoptic-scale circulation features to explain their observations: the location and strength of the subtropical anticyclone and jet stream (Montecinos and Aceituno 2003), tracks of cutoff low pressure systems (Pizarro and Montecinos 2000), strength of flow blocking in the Bellingshausen (Rutllant and Fuenzalida 1991) and Weddell Seas (Garreaud and Battisti 1999), and amplitude of midtroposphere troughs and surface lows (Barrett et al. 2011). There is also good evidence for mesoscale forcing mechanisms being important to Chilean precipitation: mountain-valley circulation and local boundary layer mixing ratio values (Garreaud 1999), local properties of zonal cross-Andes flows (Falvey and Garreaud 2007), and the degree of flow blocking and the resulting low-level barrier jet (Barrett et al. 2009). For this study, the spatial and temporal resolution of available remote sensing, reanalysis, and upper-air and surface data led us to focus on synoptic-scale circulation anomalies.

Because the MJO has some predictability (Jones et al. 2000; Kang and Kim 2010), intraseasonal forecasts of regional precipitation are now possible, especially once relationships between the MJO and relevant forcings are documented. Carrasco (2006) began this work for Chile, relating central Chile precipitation events to the MJO and concluding that precipitation between 30° and 40°S was correlated with MJO phase. He suggested that future studies clarify the relationship between synoptic-scale circulation patterns during enhanced and suppressed precipitation episodes. Toward that end, in this study we examine intraseasonal variability of precipitation and circulation over the southeast Pacific and Chile and its relationship to the MJO. The rest of this paper is organized as follows: in section 2, we discuss the surface, reanalysis, and satellite data used to determine the modulation and briefly summarize the metric used to divide the MJO into eight phases; in section 3, we present the precipitation and circulation anomalies for various MJO phases; and in section 4, we present our conclusions.

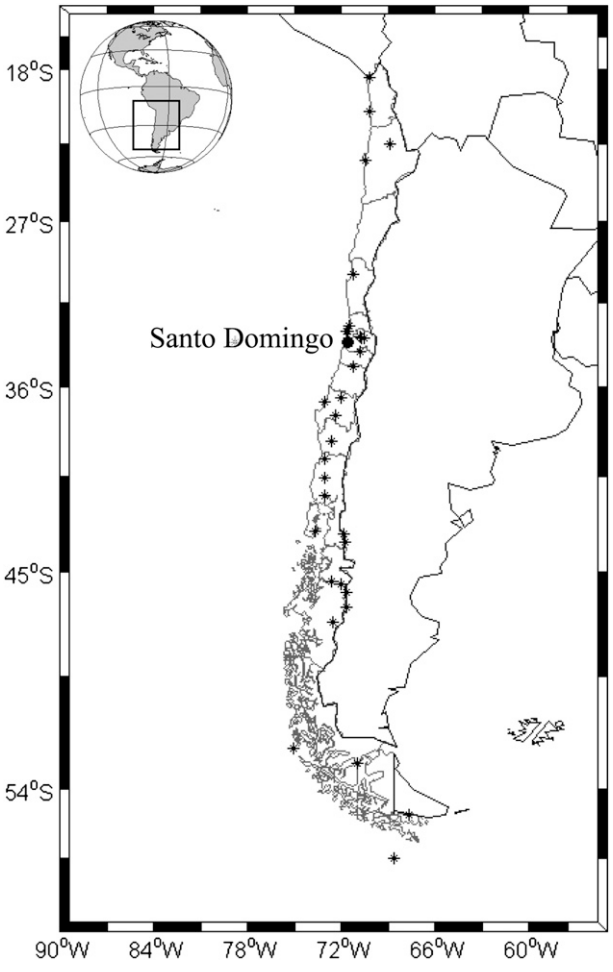

FIG. 1. Locations of surface GSOD stations (asterisks) and upper-air IGRA site (circle) used in this study.

2. Data and methods

The analyses in this study were made using five publicly-available datasets. The MJO was quantified using the

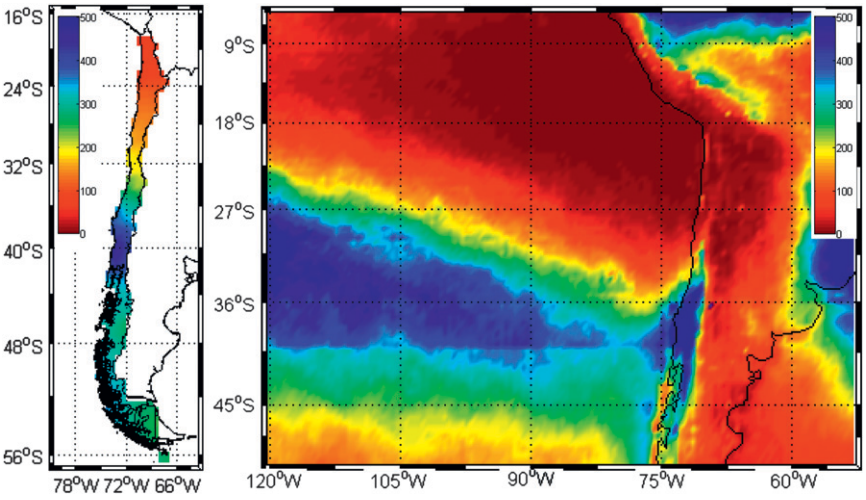

FIG. 2. Mean winter season precipitation (mm) from (left) surface GSOD data and (right) TRMM. GSOD data span from 1980 to 2010, inclusive, while TRMM data span 1999–2009. TRMM data extended to only 40°S from 1999 to 2000.

Real-Time Multivariate MJO index (RMM; Wheeler and Hendon 2004, hereafter WH04). The RMM is based on a pair of principal component time series derived from empirical orthogonal functions of near–equatorially averaged outgoing longwave radiation, 200-hPa zonal wind, and 850-hPa zonal wind. The projection of daily data onto the empirical orthogonal functions acts as an effective time filter and makes the index useful in a real-time setting. The RMM is divided into eight phases, each corresponding to a broad location of the MJO enhanced convective signal. Active MJO for this study was defined as one where the root sum of the two squared principal components, RMM1 and RMM2, was greater than one. It is interesting to note that the WH04 RMM Index has become a popular tool to examine MJO modulation of atmospheric and oceanic parameters (e.g., Deng and Jiang 2011; Ling and Zhang 2011; Martin and Schumacher 2011; and many others). A thorough description of the RMM index and several examples of its application to understanding the MJO's modulation of the atmosphere can be found in WH04.

After quantifying the MJO phase using the RMM index, atmospheric circulation and precipitation were examined using data from the National Centers for Environmental Prediction (NCEP)–Department of Energy (DOE) reanalysis 2 (Kalnay et al. 1996), the NCEP Global Summary of the Day (GSOD) precipitation database, the TRMM daily rain summary (dataset 3B42; Kummerow et al. 1998), and the NCEP Integrated Radiosonde Archive (IGRA). Winter [May–August (MJJA)] GSOD precipitation data were quality controlled to remove clearly erroneous observations, and here we caution other users of GSOD data to perform similar quality-control checks. As an example, the station at Arica [World Meteorological Organization (WMO) station 85406] in the heart of the Atacama Desert had several daily precipitation amounts of exactly 2.01″ (51.05 mm), which were not only far statistical outliers but also did not make physical sense given the hyperaridity of the region. The 34 Chilean GSOD stations are marked by crosses in Fig. 1. Irregularly spaced rain gauge data were fit to a grid in MATLAB using the gridfit tool with the springs regularizer option and smoothness parameter set to 5.

To explain the variability observed in the GSOD rainfall data, we examined the following NCEP–DOE reanalysis 2 variables: surface u, v wind; 925-hPa u, v wind; 500-hPa and 200-hPa geopotential height, 700-hPa omega, and cross-sectional relative humidity at 35°S between 100° and 50°W. In addition to surface and reanalysis data, we also examined upper-air IGRA data from the regular radiosonde station at Santo Domingo, Chile. Santo Domingo is marked with a circle in Fig. 1. The reanalysis, GSOD, and IGRA data span from 1980 to 2010, inclusively. These 31-yr datasets are especially helpful because the periodicity of the MJO means that it often only completes only a few cycles per winter. The TRMM data spanned from 1999 to 2009, inclusively. While this 11-yr dataset is shorter than the others and thus captures fewer MJO cycles, its higher-resolution (quarter-degree) coverage of the open ocean, combined with the fact that its precipitation anomalies aligned well with expected anomalies from the other datasets (i.e., negative 700-hPa omega anomalies aligned with positive TRMM rainfall anomalies), gave us confidence to use it as another tool to connect the MJO to variability.

Once the various datasets were selected, we then created composites of daily values for each variable, one composite for each of the eight phases of the MJO. Because the majority of precipitation in central Chile between 25° and 45°S falls in winter months, the daily composites consist of data from MJJA. Standardized precipitation (''normalized'') anomalies were calculated at each station by finding the mean for each MJO phase, subtracting the mean for the entire winter season, and dividing the resulting anomaly by the station standard deviation σ (Junker et al. 2008).

3. Results

a. Precipitation

The first part of this study concentrated on precipitation variability across different phases of the MJO. Because the upper-tropospheric component of the MJO circumnavigates the tropics (as a wind anomaly) and the WH04 phases were designed so that the MJO completes one oscillation on the intraseasonal (30–40 day) time scale (from phase 1 to phase 8, then back to phase 1), we expected to see similar variability in the patterns of precipitation over Chile. Rain gauge–based precipitation anomalies (Fig. 3) follow this pattern, with positive (negative) anomalies persisting for several phases before changing signs. Positive normalized rainfall anomalies between 0.1 and 0.2σ were found between 30° and 45°S during phases 8, 1, and 2, with the strongest positive anomalies in phase 2 between 35° and 45°S (Fig. 3). By phase 3, the positive anomalies had diminished considerably and were confined north of 30°S; over the rest of southern Chile, the anomalies had reversed to become negative [$(0.2–0.3)\sigma$] extending from 35° to 55°S (Fig. 3). These negative anomalies persisted from phase 3 through phase 6; however, by phase 7, new positive anomalies had appeared in the southern part of Chile (between 45° and 50°S), while the negative anomalies had diminished and were confined to between 30° and 40°S. These positive anomalies spread northward in phase 8, thus completing the cycle discussed above.

To confirm the accuracy of the GSOD rain gauge data, as well as to gain a broader perspective of rainfall anomalies and especially their spatial extent over the larger southeast Pacific region, we examined composites of TRMM data for the same eight MJO phases. It is important to note that unlike GSOD data, which span 1980–2010, TRMM data only span 1999–2009. TRMM data showed positive rainfall anomalies during phases 8 and 1 between 30° and 45°S (Fig. 4), in good agreement with the GSOD gauge-based analysis. Furthermore, strong negative precipitation anomalies in the GSOD data were found in phases 3, 4, 5, and 6 for the area between 30° and 45°S, with the strongest negative anomalies during phase 3 around 40°S, and TRMM anomalies match well with similar negative anomalies between 32° and 48°S and the strongest negative anomalies were concentrated around 40°S during phase 3 (Fig. 4). Finally, the reversal from negative to positive anomalies in GSOD data occurred in phase 7, with weak positive anomalies in southern Chile between 45° and 50°S, and this reversal was also found in the TRMM data with weak positive TRMM anomalies in the same area. The one exception to the agreement between the two datasets occurred in phase 2, where the GSOD data indicated the strong positive rainfall anomalies that were found in phases 8 and 1 would continue while the TRMM data showed a return to neutral precipitation anomalies (phase 2 in Figs. 3 and 4).

In addition to surface and remotely sensed rainfall, this study examined a longitude–height cross section of relative humidity (RH) at 35°S (Fig. 5; the cross-section location is indicated by a dashed line in Fig. 4). Relative humidity values in the lower and middle troposphere (between 500 and 1000 hPa) along and west of the Andes (topography is shown in black in Fig. 5) agreed reasonably well with the three precipitation datasets: positive TRMM and GSOD and negative OLR anomalies in phases 8 and 1 aligned with positive RH anomalies, while negative TRMM and GSOD and positive OLR anomalies aligned with negative RH anomalies in phases 4–7 (Fig. 5). High RH values in phase 2 agreed with the GSOD (rain gauge) anomaly, suggesting that the neutral TRMM anomalies underestimated precipitation in this phase.

In addition to examining standardized anomalies of precipitation, this study also examined anomalies in the frequency of heavy rainfall events, defined here as events with daily rainfall anomalies greater than 1σ at rain gauge stations in the GSOD data. The frequency of heavy rainfall events was calculated by finding the average number of winter-season days with precipitation more than 1σ above normal for each MJO phase. As expected, phases 7, 8, 1, and 2 had the highest frequency of days with more than 1σ rainfall in central and southern Chile (30°–55°S; Fig. 6). Phase 3 had a lower frequency of heavy precipitation over all of Chile, while phases 4 and 5 had low frequencies in northern Chile (15°–30°S) and moderate to higher frequencies in southern Chile (40°–55°S). Phase 6 showed moderate–high frequency over most of Chile.

b. Circulation

After quantifying precipitation variability by MJO phase, we then turned our attention to explaining the observed variability by examining anomalies in atmospheric circulation. As mentioned above, other authors have

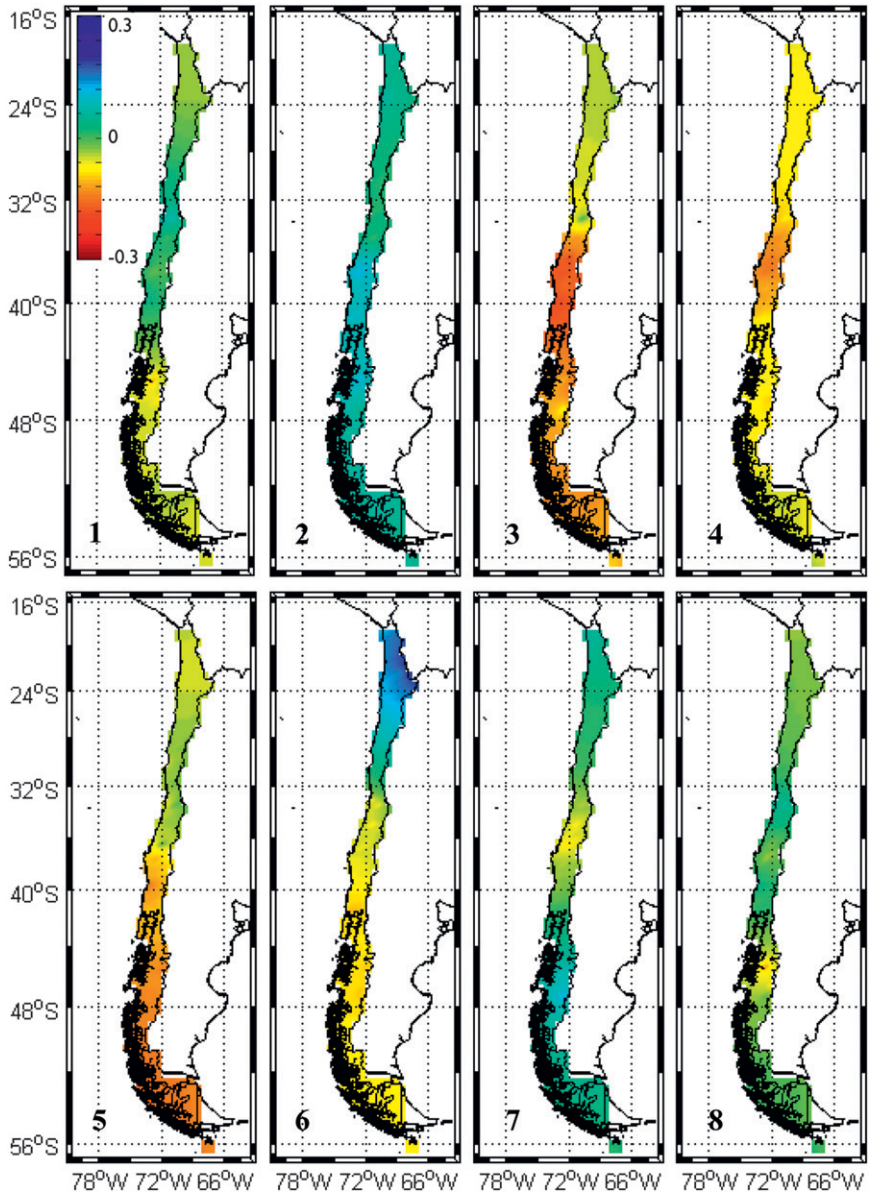

FIG. 3. Rain gauge–based precipitation standardized anomalies stratified by MJO phase: (top) (left to right) phase 1– 4 and (bottom) (left to right) phase 5–8. Positive (blue) anomalies indicate above-normal precipitation.

already documented the forcing mechanisms for precipitation in Chile, and much of their work centered on synoptic-scale forcing mechanisms. Thus, in this part of our study, we examined various synoptic-scale forcing mechanisms to determine how it also varies by MJO phase.

The first forcing mechanisms examined were mean sea level pressure and surface wind. In phase 1, weak low pressure anomalies and associated cyclonic circulation anomalies were located just west of south-central Chile, centered near 40°S, 85°W (Fig. 7). Weak surface high anomalies extended along the north-central coast, north of 30°S, and another stronger surface high anomaly was located over the southern southeast Pacific. In phase 2, the surface ridge and anticyclonic surface wind anomalies extended along the west 105th meridian over most of the southeast Pacific, and surface flow anomalies along the coast of Chile to about 35°S were southerly (Fig. 7). Another anomalous surface low was centered near 55°S, 100°W in phase 3, and in phase 4 the low pressure anomalies were centered farther east over the southern tip of Chile, with surface high anomalies extending along 120°W. In phases 5 and 6, the surface high pressure and

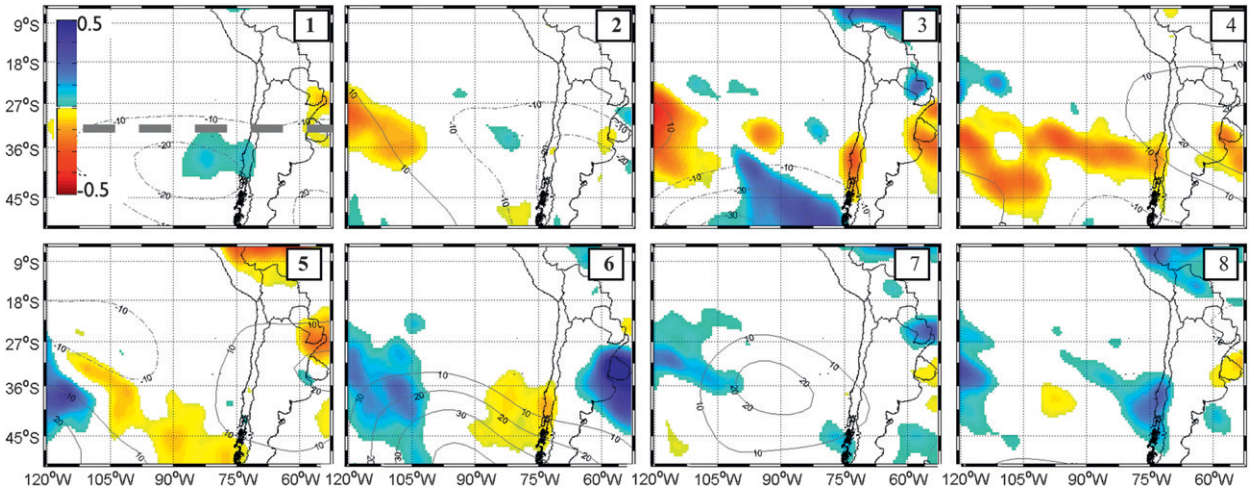

FIG. 4. TRMM precipitation anomalies (mm day^{-1}) and reanalysis 500-hPa geopotential height anomalies (contours every 10 m; negative anomalies dashed) stratified by MJO phase: (top) (left to right) phase 1– 4 and (bottom) (left to right) phase 5–8 Dashed line in phase 1 indicates location of cross section in Fig. 5. Note TRMM data span 1999–2009.

anticyclonic wind anomalies expanded greatly, covering most of the southern parts of the southeast Pacific and southern Chile. However, by phases 7 and 8, the circulation and pressure anomalies returned to cyclonic and low, respectively (Fig. 7).

The next forcing mechanisms examined were upper-level (200-hPa) geopotential height and midlevel (700-hPa) vertical velocity. In phase 1, low geopotential heights were located west of southern Chile, and negative 700-hPa omega anomalies (corresponding to rising motion) were located over and just west of Chile, between the coast and the axis of the 200-hPa height anomalies (Fig. 8). Low geopotential height anomalies and negative 700-hPa omega anomalies persisted in similar location but diminished by phases 2 and 3 (Fig. 8). By phases 4 and 5, positive upper-level height anomalies and positive 700-hPa omega anomalies began to appear over the southeast Pacific between 60°S, 120°W and 30°S, 90°W. By phase 6, large positive height omega anomalies were found over the southeast Pacific, centered near 50°S, 100°W and 40°S, 80°W, respectively. The height anomalies diminished in phases 7 and 8, and by phase 8 anomalous rising motion was found again along and west of central Chile, from 30° to 45°S (Fig. 8).

Midtropospheric height anomalies at 500 hPa were very similar to the upper-level anomalies. Low height

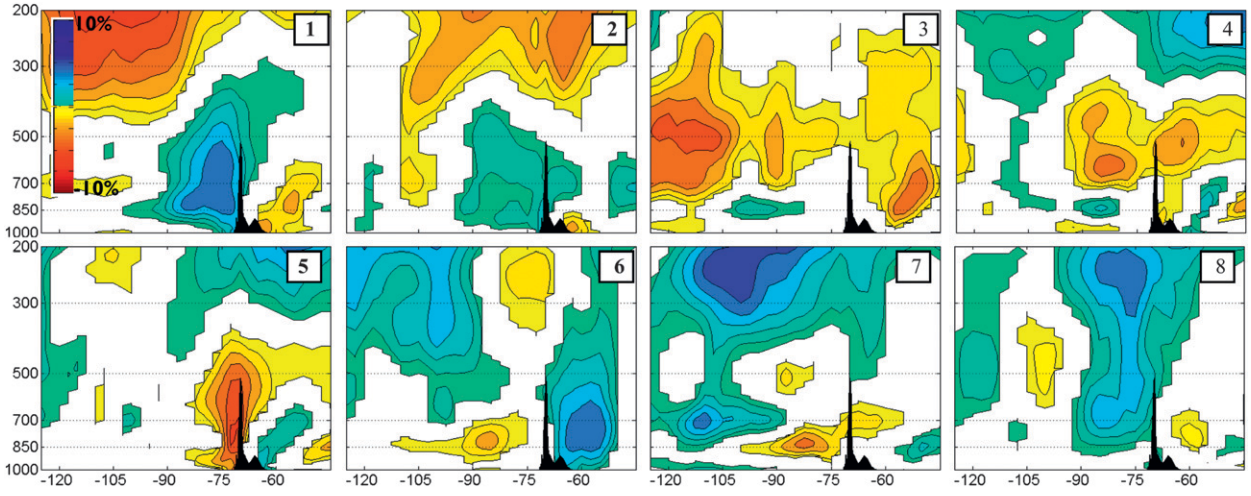

FIG. 5. Longitude–height cross section of relative humidity anomalies (in percent), stratified by MJO phase, for 32.5°–35°N: (top) (left to right) phase 1– 4 and (bottom) (left to right) phase 5–8. Black shading represents topography. Cross-section location shown by dashed line in Fig. 4 and relative humidity data from Reanalysis.

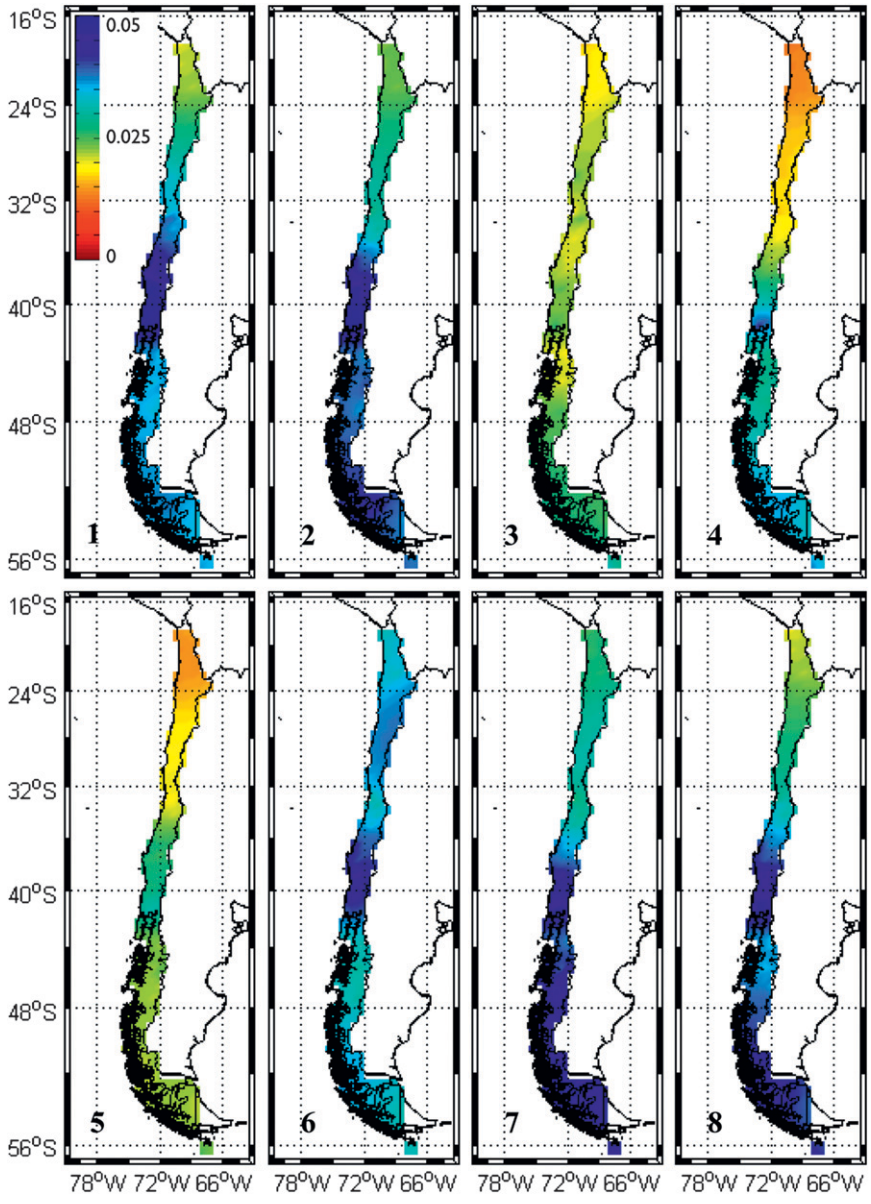

FIG. 6. Frequency of rainfall anomalies more than one standard deviation above the mean, stratified by MJO phase: (top) (left to right) phase 1– 4 and (bottom) (left to right) phase 5–8. Frequency of 0.05 implies that daily rainfall more than one standard deviation above the mean occurred during 5% of the days of that MJO phase.

anomalies over south-central Chile (30°–50°S) extending west 1000 km to 85°W existed in phases 1 and 2 (Fig. 4, contours). By phases 3 and 4, the dominant low anomaly was centered near 50°S, 100°W (phase 3) and 55°S, 75°W (phase 4). This low height anomaly reversed to become a high height anomaly in phases 5, 6, and 7, with phase 6 having the highest anomaly centered about 1000 km southwest of southern Chile. By phase 8, 500-hPa height anomalies near Chile were neutral again, leading to the negative anomaly discussed above for phase 1 (Fig. 4).

To better understand the variability of local circulation during phases of the MJO, lower-tropospheric flow (850 hPa) was examined using IGRA data at Santo Domingo. The examination of 850-hPa flow at Santo Domingo was motivated by recent studies that found that prior to and during winter precipitation events along the central Chilean coast, low-level wind speeds increased and flow direction veered to come from the north–northwest. The data at Santo Domingo showed similar results. During phase 1, a wet phase for central

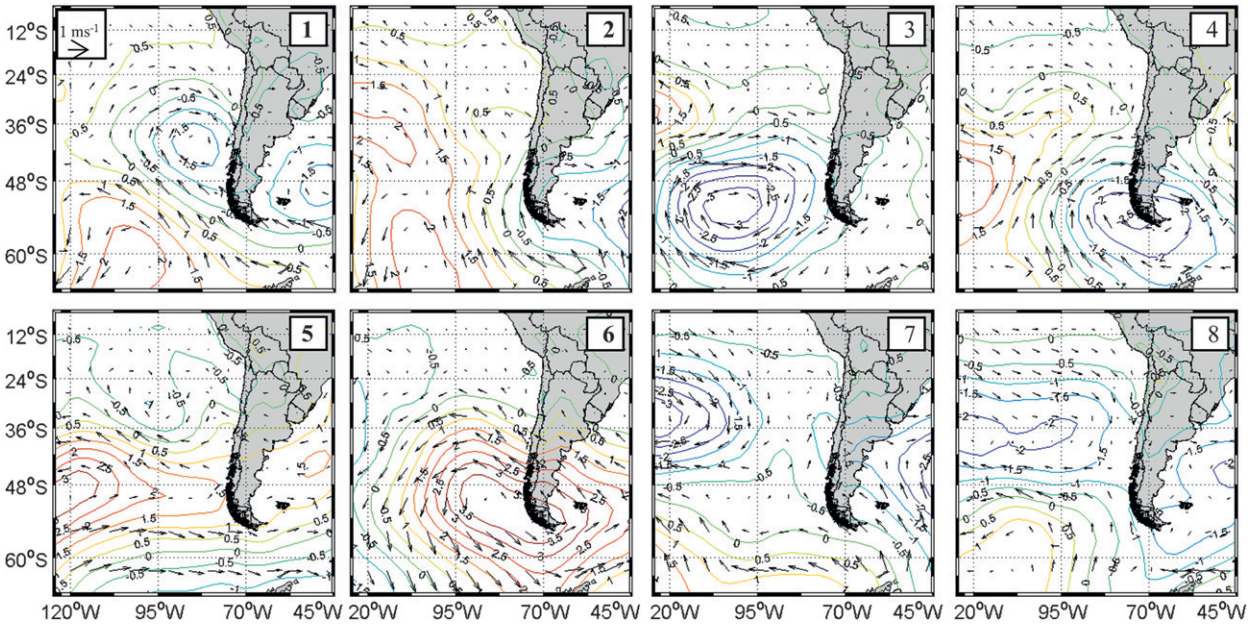

FIG. 7. Reanalysis-based sea level pressure (color contours, every 0.5 mb) and surface wind anomalies. Red (blue) colors are positive (negative) anomalies: (top) (left to right) phase 1– 4 and (bottom) (left to right) phase 5–8.

Chile (30°–40°S), wind direction was predominantly north–northwesterly and maximum speeds exceeded 20 m s^{-1} (Fig. 9). In contrast, during phase 4, the driest phase for central Chile, the dominant wind direction was south–southeasterly with only a few maximum speeds greater than 10 m s^{-1}.

4. Discussion

The primary objectives of this study were to examine variability of precipitation in Chile by phase of the MJO and then explain the observed variability by examining composite anomalies of atmospheric circulation: surface

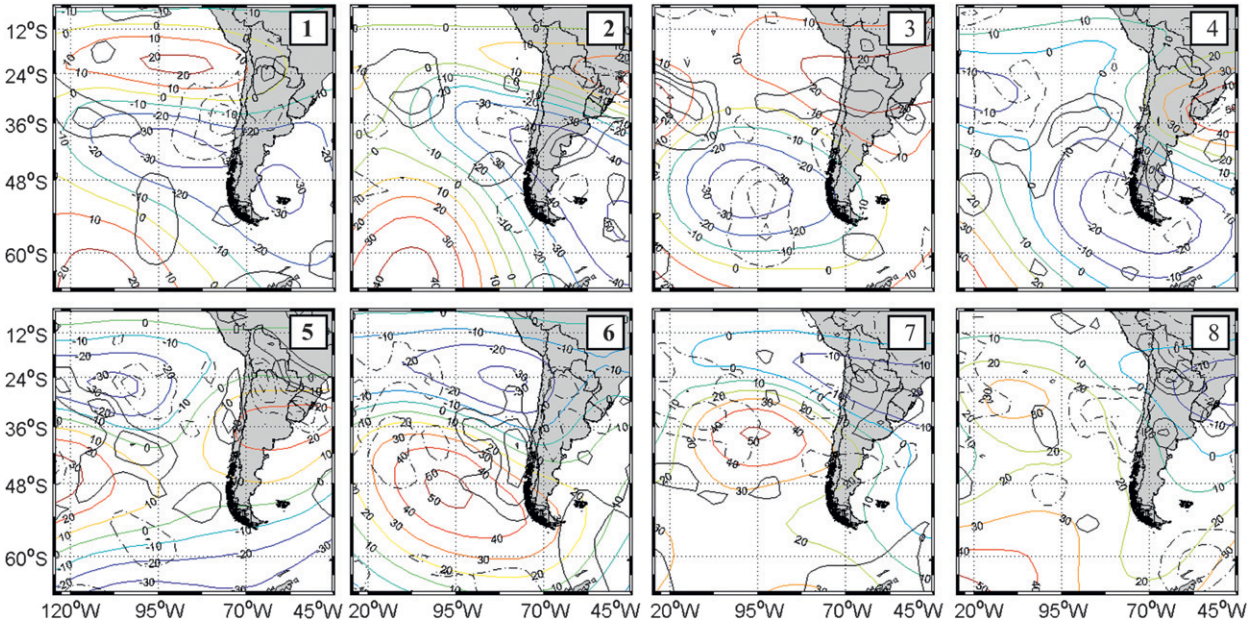

FIG. 8. Anomalies of 200-hPa geopotential height (color contours, m) and 700-hPa omega (pressure-coordinate vertical velocity, mb h^{-1}) by MJO phase: (top) (left to right) phase 1– 4 and (bottom) (left to right) phase 5–8. Red (blue) colors are positive (negative) anomalies, and negative omega anomalies (indicating upward motion) are dashed. Data are from Reanalysis.

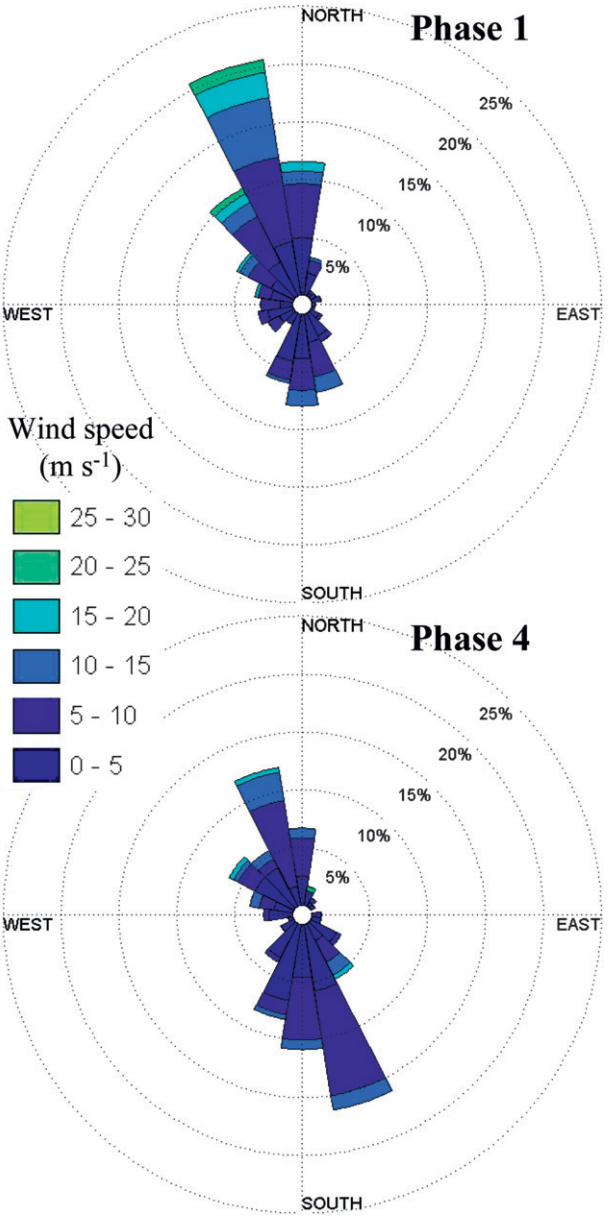

FIG. 9. Direction and speed variability in 850-hPa wind at Santo Domingo (see Fig. 1) for MJO (top) phase 1 and (bottom) phase 4.

sea level pressure, surface flow, 850-hPa horizontal flow, 700-hPa vertical velocity, 500-hPa geopotential height, and 200-hPa geopotential height. Anomalies in synoptic-scale circulation and geopotential height agreed well with anomalies in precipitation. Both of the separate measures of precipitation, TRMM and GSOD, were in agreement, indicating positive precipitation anomalies over much of southern and central Chile during MJO phases 8 and 1 and negative anomalies during phases 3–6. The measures also agreed for an area of positive rainfall anomalies in southern Chile in phase 7. A cross section of relative humidity anomalies through 35°S agreed with these precipitation anomalies, with strong positive relative humidity anomalies during phases 8, 1, and 2 along and upstream of the Andes during phases of above-normal precipitation, and negative upstream relative humidity anomalies during phases 4, 5, 6, and 7. Anomalies in the frequency of heavier precipitation events (Fig. 6), defined by the frequency of anomalies greater than 1 standard deviation from the mean, agreed well with standardized anomalies (Fig. 3). For central and southern Chile, the phases with greater frequency of heavy rain events (phases 8, 1, and 2) were also the rainier phases. This agreement indicates that the wetter phases were often characterized by heavier precipitation events as well. Similarly, the drier phases, especially phases 3 and 5 in southern Chile, tended to have lower frequency of heavy precipitation events. Northern Chile, where both mean and standard deviations in precipitation are small, showed an interesting result. phase 6 had relatively high standardized anomalies as well as frequency of heavy events. A closer inspection revealed that the high-altitude (eastern) station received substantial rainfall, including several daily amounts more than 1σ above normal, during phase 6. However, this rainfall pattern only existed at the high-altitude station, resulting in a very tight gradient between it and the rain-free coastal (western) stations. This gradient was smoothed by the gridfit interpolation scheme, producing the result seen in Fig. 6.

Surface pressure anomalies were also in good agreement with the precipitation anomalies: general lower pressures (negative anomalies) between 30° and 45°S along and west of Chile were found during rainy phases, with neutral to higher pressure anomalies during phases with negative precipitation anomalies. Lower-troposphere circulation anomalies also agreed well, with northerly wind anomalies during phases with positive precipitation anomalies (especially over south-central Chile from 35° to 45°S) and southerly wind anomalies during phases with negative precipitation anomalies. One exception to this pattern was observed in phase 7, with southerly wind anomalies collocated with a positive rainfall anomaly. Negative middle- and upper-tropospheric height anomalies along and west of Chile existed during phases with above-normal precipitation, and positive height anomalies corresponded with periods of below-normal precipitation. Middle-troposphere vertical motion also agreed well with both precipitation and height anomalies, with upward vertical velocity anomalies collocated with positive precipitation anomalies and located along and east of negative height anomalies. Downward vertical velocity anomalies corresponded as well, collocated with positive precipitation anomalies and downstream of positive height anomalies.

Besides their agreement with precipitation, the surface pressure and middle-, and upper-tropospheric geopotential height anomalies in Figs. 4, 7, and 8 together show a classic equivalent barotropic wave train. While the wave train is more prominent in some phases than others, particularly strong signals appear in the 200-hPa anomalies in phases 1, 2, 3, and 6. High and low anomaly centers are spaced approximately 3000 km apart, with minimal tilt with height. These results agree well with the observational and modeling studies of Berbery et al. (1992) and Mechoso et al. (1991) and the theoretical findings of Hoskins and Karoly (1981) and Bladé and Hartmann (1995), indicating a teleconnection response to deep convective activity in the Maritime Continent. The origin of this observed wave train and a possible pathway to the Southern Hemisphere extratropics was explained by Sardeshmukh and Hoskins (1988), who noted that a divergence field in easterly flow asymmetric about the equator led to an extremely effective Rossby wave source in the subtropical westerlies.

Finally, point circulation measures from upper-air data at Santo Domingo reveal that the variability in both speed and direction also agree well with rainfall anomalies. The 850-hPa circulation during phase 1 included a significant northerly component, and with faster speeds, than at phase 4 (whose directional mode was southerly and at slower speeds), agreeing well with the local meridional flow maximum observed by Barrett et al. (2009) during a rain event. This result suggests additional work is needed to further explore possible mesoscale impacts of the MJO, as the low-level flow data are likely sampling a barrier jet that developed in response to flow blocking during the approach of a midlatitude cyclone. Such a study could examine local modulation of Froude numbers, in addition to mesoscale circulations, as these are also important to precipitation.

Acknowledgments. Partial funding for this work was made possible from a grant to the U.S. Naval Academy via the Office of Naval Research. We would also like to thank the helpful and constructive comments from two anonymous reviewers and Dr. B. Liebmann.

REFERENCES

Barrett, B. S., R. Garreaud, and M. Falvey, 2009: Effect of the Andes cordillera on precipitation from a midlatitude cold front. *Mon. Wea. Rev.,* **137,** 3092–3109.

——, D. B. Krieger, and C. P. Barlow, 2011: Multiday observational climatology for rain events in central Chile. *J. Hydrometeor.,* **12,** 1071–1085.

Berbery, E. H., J. Nogués-Paegle, and J. D. Horel, 1992: Wavelike Southern Hemisphere extratropical teleconnections. *J. Atmos. Sci.,* **49,** 155–177.

Bladé, I., and D. L. Hartmann, 1995: The linear and nonlinear extratropical response of the atmosphere to tropical intraseasonal heating. *J. Atmos. Sci.,* **52,** 4448–4471.

Carrasco, J. F., 2006: Precipitation events in central Chile and its relation with the MJO. *Proc. Eighth Int. Conf. on Southern Hemisphere Meteorology and Oceanography,* Foz do Iguacu, Brazil, Amer. Meteor. Soc., 1719–1722.

Deng, Y., and T. Jiang, 2011: Intraseasonal modulation of the North Pacific storm track by tropical convection in boreal winter. *J. Climate,* **24,** 1122–1137.

Donald, A., H. Meinke, B. Power, A. de H. N. Maia, M. C. Wheeler, N. White, R. C. Stone, and J. Ribbe, 2006: Near-global impact of the Madden–Julian oscillation on rainfall. *Geophys. Res. Lett.,* **33,** L09704, doi:10.1029/2005GL025155.

Falvey, M., and R. Garreaud, 2007: Wintertime precipitation episodes in central Chile: Associated meteorological conditions and orographic influences. *J. Hydrometeor.,* **8,** 171–193.

Garreaud, R., 1999: A multiscale analysis of the summertime precipitation over the central Andes. *Mon. Wea. Rev.,* **127,** 901–921.

——, 2009: The Andes climate and weather. *Adv. Geosci.,* **7,** 1–9.

——, and D. S. Battisti, 1999: Interannual (ENSO) and interdecadal (ENSO-like) variability in the Southern Hemisphere tropospheric circulation. *J. Climate,* **12,** 2113–2123.

——, A. Molina, and M. Farias, 2010: Andean uplift and Atacama hyperaridity: A climate modeling perspective. *Earth Planet. Sci. Lett.,* **292,** 39–50.

Hoskins, B. J., and D. J. Karoly, 1981: The steady linear response of a spherical atmosphere to thermal and orographic forcing. *J. Atmos. Sci.,* **38,** 1179–1196.

Jeong, J.-H., B.-M. Kim, C.-H. Ho, and Y.-H. Noh, 2008: Systematic variation in wintertime precipitation in East Asia by MJO-induced extratropical vertical motion. *J. Climate,* **21,** 788–801.

Jones, C., D. E. Waliser, J. K. Schemm, and W. K. Lau, 2000: Prediction skill of the Madden–Julian oscillation in dynamical extended range forecasts. *Climate Dyn.,* **16,** 273–289.

——, J. Gottschalck, L. M. V. Carvalho, and W. R. Higgins, 2011: Influence of the Madden–Julian oscillation on forecasts of extreme precipitation in the contiguous United States. *Mon. Wea. Rev.,* **139,** 332–350.

Junker, N. W., R. H. Grum, R. Hart, L. F. Bosart, K. M. Bell, and F. J. Pereira, 2008: Use of normalized anomaly fields to anticipate extreme rainfall in the mountains of northern California. *Wea. Forecasting,* **23,** 336–356.

Kalnay, E., and Coauthors, 1996: The NCEP/NCAR 40-Year Reanalysis Project. *Bull. Amer. Meteor. Soc.,* **77,** 437–471.

Kang, I.-S., and H.-M. Kim, 2010: Assessment of MJO predictability for boreal winter with various statistical and dynamical models. *J. Climate,* **23,** 2368–2378.

Krishnamurti, T. N., P. K. Jayakumar, J. Sheng, N. Surgi, and A. Kumar, 1985: Divergent circulations on the 30–50-day time scale. *J. Atmos. Sci.,* **42,** 364–375.

Kummerow, C., W. Barnes, T. Kozu, J. Shiue, and J. Simpson, 1998: The Tropical Rainfall Measuring Mission (TRMM) sensor package. *J. Atmos. Oceanic Technol.,* **15,** 809–817.

Ling, J., and C. Zhang, 2011: Structural evolution in heating profiles of the MJO in global reanalyses and TRMM retrievals. *J. Climate,* **24,** 825–842.

Madden, R. A., and P. R. Julian, 1971: Detection of a 40–50-day oscillation in the zonal wind in the tropical Pacific. *J. Atmos. Sci.,* **28,** 702–708.

——, and ——, 1972: Description of global-scale circulation cells in the tropics with a 40–50-day period. *J. Atmos. Sci.,* **29,** 1109–1123.

Martin, E. R., and C. Schumacher, 2011: Modulation of Caribbean precipitation by the Madden–Julian oscillation. *J. Climate,* **24,** 813–824.

Matthews, A. J., 2000: Propagation mechanisms for the Madden–Julian oscillation. *Quart. J. Roy. Meteor. Soc.,* **126,** 2637–2651.

Mechoso, C. R., J. D. Farrara, and M. Ghil, 1991: Intraseasonal variability of the winter circulation in the Southern Hemisphere atmosphere. *J. Atmos. Sci.,* **48,** 1387–1404.

Montecinos, A., and P. Aceituno, 2003: Seasonality of the ENSO-related rainfall variability in central Chile and associated circulation anomalies. *J. Climate,* **16,** 281–296.

Nogués-Paegle, J., B.-C. Lee, and V. E. Kousky, 1989: Observed modal characteristics of the intraseasonal oscillation. *J. Climate,* **2,** 496–507.

Pizarro, J. G., and A. Montecinos, 2000: Cutoff cyclones off the subtropical coast of Chile. *Proc. Sixth Int. Conf. on Southern Hemisphere Meteorology and Oceanography,* Santiago, Chile, Amer. Meteor. Soc., 278–279.

Rutllant, J., and H. Fuenzalida, 1991: Synoptic aspects of the central Chile rainfall variability associated with the Southern Oscillation. *Int. J. Climatol.,* **11,** 63–76.

Sardeshmukh, P. D., and B. J. Hoskins, 1988: The generation of global rotational flow by steady idealized tropical divergence. *J. Atmos. Sci.,* **45,** 1228–1251.

Smith, R. B., and J. P. Evans, 2007: Orographic precipitation and water vapor fractionation over the southern Andes. *J. Hydrometeor.,* **8,** 3–19.

Wheeler, M. C., and H. H. Hendon, 2004: An all-season real-time multivariate MJO index: Development of an index for monitoring and prediction. *Mon. Wea. Rev.,* **132,** 1917–1932.

——, ——, S. Cleland, H. Meinke, and A. Donald, 2009: Impacts of the Madden–Julian oscillation on Australian rainfall and circulation. *J. Climate,* **22,** 1482–1498.

Zhang, C., 2005: Madden–Julian oscillation. *Rev. Geophys.,* **43,** 1–36.